

Communication

# In Situ Wet Etching of MoS<sub>2</sub>@dWO<sub>3</sub> Heterostructure as Ultra-Stable Highly Active Electrocatalyst for Hydrogen Evolution Reaction

Xintian Liu and Congwei Wang \*

CAS Key Laboratory of Carbon Materials, Institute of Coal Chemistry, Chinese Academy of Sciences, Taiyuan 030001, China; liuxintian@sxicc.ac.cn

\* Correspondence: wangcongwei@sxicc.ac.cn; Tel.: +86-351-4040131

Received: 20 July 2020; Accepted: 15 August 2020; Published: 31 August 2020



**Abstract:** Electrocatalysts featuring robust structure, excellent catalytic activity and strong stability are highly desirable, but challenging. The rapid development of two-dimensional transition metal chalcogenide (such as WO<sub>3</sub>, MoS<sub>2</sub> and WS<sub>2</sub>) nanostructures offers a hopeful strategy to increase the active edge sites and expedite the efficiency of electronic transport for hydrogen evolution reaction. Herein, we report a distinctive strategy to construct two-dimensional MoS<sub>2</sub>@dWO<sub>3</sub> heterostructure nanosheets by in situ wet etching. Synthesized oxygen-incorporated MoS<sub>2</sub>-was loaded on the surface of defective WO<sub>3</sub> square nanoframes with abundant oxygen vacancies. The resulting nanocomposite exhibits a low overpotential of 191 mV at 10 mA cm<sup>-2</sup> and a very low Tafel slope of 42 mV dec<sup>-1</sup> toward hydrogen evolution reaction. The long-term cyclic voltammetry cycling of 5000 cycles and more than 80,000 s chronoamperometry tests promises its outstanding stability. The intimate and large interfacial contact between MoS<sub>2</sub> and WO<sub>3</sub>, favoring the charge transfer and electron-hole separation by the synergy of defective WO<sub>3</sub> and oxygen-incorporated MoS<sub>2</sub>, is believed the decisive factor for improving the electrocatalytic efficiency of the nanocomposite. Moreover, the defective WO<sub>3</sub> nanoframes with plentiful oxygen vacancies could serve as an anisotropic substrate to promote charge transport and oxygen incorporation into the interface of MoS<sub>2</sub>. This work provides a unique methodology for designing and constructing excellently heterostructure electrocatalysts for hydrogen evolution reaction.

**Keywords:** transition-metal chalcogenide; heterostructure; in situ etching; hydrogen evolution reaction

---

## 1. Introduction

Electrocatalysts water-splitting product hydrogen is reproducible and clean energy [1–3]. The development of platinum (Pt)-free electrocatalysts is a crucial problem to improve the generally efficiency for hydrogen evolution reaction (HER), especially when facing resources shortage and energy crisis [4–6]. Newly, two-dimensional (2D) transition metal chalcogenides have always been mentioned, such as molybdenum disulfide (MoS<sub>2</sub>) [7,8], tungsten oxide (WO<sub>3</sub>) [9,10], molybdenum selenide (MoSe<sub>2</sub>) [11,12] and can demonstrated to clarify the mechanism for HER in strong acids. For instance, MoS<sub>2</sub> has great potential as an alternative to Pt for catalyzing overall water-splitting cost-effectively and efficiently [13–16]. Theoretical studies have shown that along the edges of 2D MoS<sub>2</sub> nanosheets is the source of highly HER, which plays a crucial role in constructing hybrid catalyst [15,17,18]. Therefore, the development of MoS<sub>2</sub> based catalysts, featuring rich active edge sites [19] and accessible surface areas [20], is of vital significance to improve the overall efficiency for HER. Though many literatures have been reported the great potential of MoS<sub>2</sub> as HER electrocatalyst [3,21,22], the severe stacking of

MoS<sub>2</sub> nanosheets during the preparation and electrochemical reaction process significantly impact its stability and hinders its application compared with Pt-based electrocatalysts [21,23]. Therefore, unless the electronic structure can be appropriately modulated by varying the chemical constituents [18] to increase the population of active sites [17] or introducing durable supportive materials [5,24] to prevent the aggregation, the 2D layered MoS<sub>2</sub> could hardly be employed into practical application without long-term stability [25].

Tungsten trioxide (WO<sub>3</sub>) is another distinctive 2D layered oxide [26] with faster proton insertion kinetics than other two-dimensional transition metal chalcogenides, attributing to its larger proton diffusion coefficient [9]. Recently, improving the HER performance by designing and constructing various nanostructure components has been considered an available strategy to remarkably increase the active edge sites [25,27] and improve the long-term stability [28]. Indeed, researchers have reported that regulating the interlayer spacing of MoS<sub>2</sub> nanosheets by forming hetero-structure can optimize the HER performance [29–31]. For example, Lan and coworkers synthesized a molybdenum disulfide/nitrogen-doped reduced graphene oxide (MoS<sub>2</sub>/N-RGO) hetero-composite and found that the enlarged interlayer spacing of MoS<sub>2</sub> is beneficial to improve HER performance [32]. Because of the unique 2D ultra-thin layered morphology, which ensure the ultra-fast electron transfer, the MoS<sub>2</sub>/N-RGO exhibited excellent catalytic activity with a lower onset potential, lower Tafel slope, larger current density and good stability over 5000 cycles. Moreover, Wang reported a newly strategy to construct well-defined W<sub>17</sub>O<sub>47</sub>–MoS<sub>2</sub> heterostructure catalyst with clear interface. By constructing heterostructure, it is possible to create highly accessible anion-deficit sites for precise electronic structures and intimate hetero-interface for spatial charge-flow steering [18]. The W<sub>17</sub>O<sub>47</sub>–MoS<sub>2</sub> composite shows that the mass activity of MoS<sub>2</sub> is 116 times higher than pure MoS<sub>2</sub>. Therefore, the structural combination of different nanostructures, leaded to more active edge sites [33,34] and enlarged interlayer spacing of MoS<sub>2</sub> [35,36], is demonstrated to be an effective approach to improve the HER activity. In this regard, rational design and further synthesis of MoS<sub>2</sub>-based catalysts with low-dimensional constrains and thermodynamic limitations between two completely different compounds are highly desirable, but also challenging.

Herein, we demonstrate an *in situ* wet etching method by growing the oxygen-incorporated 2D MoS<sub>2</sub> nanosheets on defective WO<sub>3</sub> nanoframes (denoted as MoS<sub>2</sub>@dWO<sub>3</sub>) to form a unique two-dimensional heterostructure. The defective WO<sub>3</sub> nanoframes with abundant oxygen vacancies serve as an anisotropic substrate to promote charge transport and carrier injection into the interface of MoS<sub>2</sub> nanosheets [37], while 2D MoS<sub>2</sub> nanosheets provide highly active sites on edges for HER. The resulting hetero-catalyst exhibits highly activity with a low overpotential of 191 mV at 10 mA cm<sup>-2</sup>, with a Tafel slope of 42 mV dec<sup>-1</sup> toward hydrogen evolution reaction. The long-term cyclic voltammetry cycling of 5000 cycles and more than 80,000 s chronoamperometric (CA) tests promises its outstanding stability. The success synthesis of MoS<sub>2</sub>@dWO<sub>3</sub> via the construction of 2D heterostructure through defects-engineering (*in situ* wet etching) will provide unique pathways for pursuing efficient electrocatalysts for energy storage and conversion.

## 2. Results and Discussion

The MoS<sub>2</sub>@dWO<sub>3</sub> heterostructure nanosheets were prepared by *in situ* wet etching of presynthesized WO<sub>3</sub> nanosheets at the presence of Mo-based etching agent. The pure WO<sub>3</sub> nanosheets exhibited a uniform square of 100–120-nm lateral size and 8–10-nm-thickness with a relative smooth and regular surface morphology, as shown in Figure 1a. After the *in situ* etching, transmission electron microscope (TEM) image shown that a heterostructure hollow 2D MoS<sub>2</sub>@dWO<sub>3</sub> nanoframe with uniform shape and size was prepared (Figure 1b). In addition, the MoS<sub>2</sub> sheets were grown on the main body of WO<sub>3</sub> nanoframe through the thermolysis of (NH<sub>4</sub>)<sub>2</sub>MoS<sub>4</sub> in DMF at hydrothermal process of 180 °C for 10 h. Ultrasmall (10 ± 1 nm) multilayer (3–6 layers) MoS<sub>2</sub> sheets were *in situ* grown up the surface of relatively large WO<sub>3</sub> nanoframe to construct MoS<sub>2</sub>@dWO<sub>3</sub> heterostructure. It is worth nothing that the excessive use of glucose and citric acid in the synthesis process can ensure

the formation of uniform 2D square nanoframe morphology of  $\text{WO}_3$  and can also reduce the interface energy to promote the subsequent growth of  $\text{MoS}_2$ . Though delicate control of  $\text{WO}_3/(\text{NH}_4)_2\text{MoS}_4$  mass ratio and etching time, the load in this 2D heterostructure was systematically optimized.

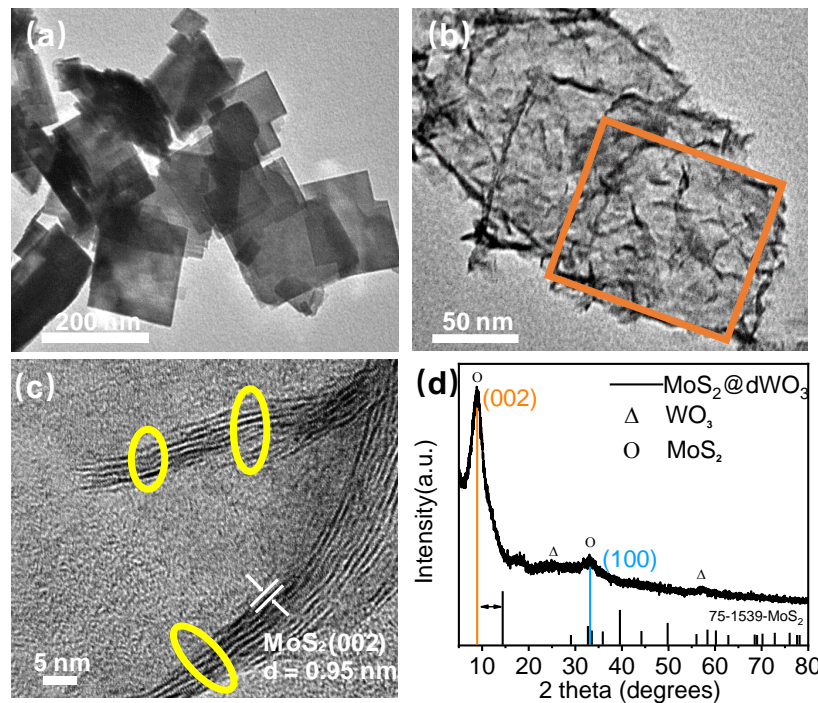
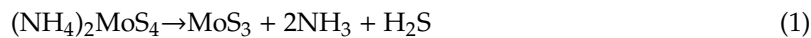


**Figure 1.** Synthesis and structure characterization. (a) TEM image of pure tungsten oxide ( $\text{WO}_3$ ); (b) TEM image of  $\text{MoS}_2@\text{dWO}_3$ . At the image, the orange circle indicated frame of  $\text{WO}_3$ ; (c) HRTEM image of  $\text{MoS}_2@\text{dWO}_3$ . At the image, the yellow circle indicates the active edges of  $\text{MoS}_2$ ; (d) XRD patterns of  $\text{MoS}_2@\text{dWO}_3$  heterostructures nanosheets.

The morphology and subtle structural evolution of the as-prepared  $\text{MoS}_2@\text{dWO}_3$  catalyst were also observed by high resolution transmission electron microscopy (HRTEM). Comparing to the direct thermolysis of  $(\text{NH}_4)_2\text{MoS}_4$  to give relatively large  $\text{MoS}_2$  nanosheets of  $\sim 200$  nm, as shown in Figure S2, the introduction of  $\text{WO}_3$  sheets as template substrate could significantly restrain the lateral growth of  $\text{MoS}_2$  nanosheets around 10 nm, offering abundant active edge sites as potential catalytic centers for HER. Meanwhile, the high crystalline solid 2D  $\text{WO}_3$  nanosheets have been simultaneously etched to form hollow square nanoframes accompanied the hydrothermal reaction of  $(\text{NH}_4)_2\text{MoS}_4$ . As shown in Figure 1c, the high magnification lattice fringes of  $\text{MoS}_2@\text{dWO}_3$  exhibited an enlarged interlayer spacing of 0.95 nm for (002)  $\text{MoS}_2$ , which is considerably different from pure  $\text{MoS}_2$  with a conventional interlayer spacing of 0.62 nm. The  $\text{MoS}_2@\text{dWO}_3$  heterostructure nanosheets were prepared by in situ wet etching of  $\text{WO}_3$  nanosheets by  $(\text{NH}_4)_2\text{MoS}_4$  in the solution of dimethylformamide (DMF), as shown in Equation (1) [38]. The intimate and large interfacial contact between  $\text{MoS}_2$  and  $\text{WO}_3$ , favoring the promoted charge transfer and electron–hole separation by the synergy of defective  $\text{WO}_3$  and  $\text{MoS}_2$ , is believed the decisive factor for improving the electrocatalytic efficiency of the nanocomposite. Specifically, the pyrolysis of  $(\text{NH}_4)_2\text{MoS}_4$  in DMF environment, produces  $\text{MoS}_3$  with a strong reducibility (Equation (2)), which makes the  $\text{WO}_3$  nanosheets etched to form a nanoframe, and abundant oxygen vacancies are generated. As an anisotropic substrate,  $\text{WO}_3$  is conducive to charge transport and carrier injection into the interface of  $\text{MoS}_2$ . Meanwhile, controllable disorder engineering of layered  $\text{MoS}_2$  by oxygen incorporation to enlarge their interlayer spacing, providing

plenty of unsaturated sulfur atoms as active sites for HER [39] and effectively regulating the electronic structure [40,41] of this nanocomposite to further enhance the intrinsic conductivity.



At the same time, the material structure of  $MoS_2@dWO_3$  was further characterized via XRD. As shown in Figure 1d, the XRD pattern of  $MoS_2@dWO_3$  is markedly different from that of pure 2H- $MoS_2$  (JCPDS No. 75-1539). After the formation of heterostructure, the nanocomposite showed a prominent (002) peak come out at the low-angle region at  $9.3^\circ$ , corresponding to a *d* spacing of  $9.5\text{ \AA}$ , verified the increased interlayer spacing from observed TEM image. In addition, a broadened peak at high angle region ( $33^\circ$ ) corresponds to the (100) planes of the pristine  $MoS_2$ , indicating the similarly atomic arrangement along the basal planes. Therefore, it can be inferred from the above characterization that the main reason for the enlarged interlayer spacing of  $MoS_2@dWO_3$  is due to the oxygen incorporation. It is noted that both theoretical and experimental studies have implied that the  $MoS_2$  with an enlarged interlayer spacing can present a more preferable free energy change for hydrogen adsorption ( $\Delta G_H$ ) and exhibits more short-range disordering than the general  $MoS_2$ -with an interlayer spacing of  $6.2\text{ \AA}$ , favoring the ultrafast kinetics process of HER [15,36,42].

Chemical state and electronic properties of the catalyst surface was further detected by X-ray photoelectron spectrum (XPS). As shown in Figure 2, XPS survey scan confirmed the presence of W, Mo, O and S elements in  $MoS_2@dWO_3$  heterostructure. Compared with pure  $WO_3$ , a distinctive new peak assigned to  $W^{4+} 4f_{7/2}$  was appeared around  $32.5\text{ eV}$ , indicating that the wet etching of pristine  $WO_3$  would induce the electron transfer from oxygen vacancies to tungsten cations on the defective  $WO_3$  surface (Figure 2a). Moreover, a positive shift and peak broadening of both  $W^{6+} 4f_{7/2}$  and  $W^{6+} 4f_{5/2}$  demonstrates the electron modulation and recombination of different compound between defective  $WO_3$  and in situ grown  $MoS_2$  [43]. In Figure 2b, the Mo 3d XPS spectrum of  $MoS_2@WO_3$  had two characteristic peaks of  $Mo^{4+} 3d_{3/2}$  ( $231.75\text{ eV}$ ) and  $Mo^{4+} 3d_{5/2}$  ( $228.65\text{ eV}$ ), indicating the dominance of  $MoS_2$  in the product. However, the enhanced peak of  $Mo^{6+} 3d_{5/2}$  ( $232.63\text{ eV}$ ) and  $Mo^{6+} 3d_{3/2}$  ( $235.73\text{ eV}$ ) represents the formation of Mo–O bonds [32,44], verifying that the oxygen was incorporated into  $MoS_2$ -layer to generate the interlayer disorder, which also corresponds to the peak shift of S. As shown in Figure 2c, the O 1s spectrum revealed the existence of W–O–W ( $530.53\text{ eV}$ ) and O-vacancies ( $531.68\text{ eV}$ ) [18] in  $MoS_2@dWO_3$ . The increase of O-vacancies peak area indicates the enhancement of O-vacancies after the formation of heterostructure. Meanwhile, the appearance of new peak at  $533.46\text{ eV}$  is ascribed to Mo–O bond, indicating a certain amount of oxygen atoms were incorporated into the layered  $MoS_2$  structure. The C–OH peak in the O 1s spectrum mainly comes from the glucose ligand on the surface. All the positions of S  $2p_{1/2}$ , S  $2p_{3/2}$  peak were in accordance with the previous literature (Figure 2d) [24]. However, we observed that the peak of  $S^{2-} 2p_{3/2}$  have  $0.05\text{ eV}$  shift toward low blinding energy, which indicated that S became easier to obtain electrons after forming heterostructure [45] and also confirmed peak of  $Mo^{6+} 3d_{5/2}$  ( $232.63\text{ eV}$ ) and  $Mo^{6+} 3d_{3/2}$  ( $235.73\text{ eV}$ ) were further enhanced because of the conservation of gain and loss electrons [5]. In summary, formation of heterostructure caused the increase of O-vacancies on the defective  $WO_3$  surface and the generation of Mo–O bond by oxygen incorporation into  $MoS_2$  layer.

In order to assess HER performance of  $MoS_2@dWO_3$  heterostructure catalyst, the electrocatalytic measurements were carried out using a standard three-electrode cell in  $N_2$ -saturated  $0.5\text{-M } H_2SO_4$  electrolyte. Linear-sweep voltammetry (LSV) curves of  $MoS_2@dWO_3$  heterostructure catalyst, control samples of pristine  $WO_3$  and pure  $MoS_2$  are shown in Figure 3a. Pristine  $WO_3$  demonstrates the most limited HER activity reflected by the low current density, attributing to the lack of active sites and its poor conductivity. The pure  $MoS_2$  exhibited significantly better activity than the pure  $WO_3$ , as exhibiting an overpotential of  $210\text{ mV}$  at  $10\text{ mA cm}^{-2}$ . The improved activity of  $MoS_2$  originated from the active-edge sites of 2D  $MoS_2$  nanosheets. The  $MoS_2@dWO_3$  heterostructure catalyst was shown the

most active catalyst, reaching the highest activity with an overpotential of 191 mV at 10 mA cm<sup>-2</sup> and the lowest Tafel slope of 42 mV dec<sup>-1</sup>, as shown in Figure 3b. The much improved activity could be attributed to the in situ grown ultrasmall MoS<sub>2</sub> nanosheets, more specifically, the oxygen-incorporated MoS<sub>2</sub> active edge sites, plus the synergistic effects brought by the intimate and large interfacial contact between defective WO<sub>3</sub> and oxygen-incorporated MoS<sub>2</sub>.

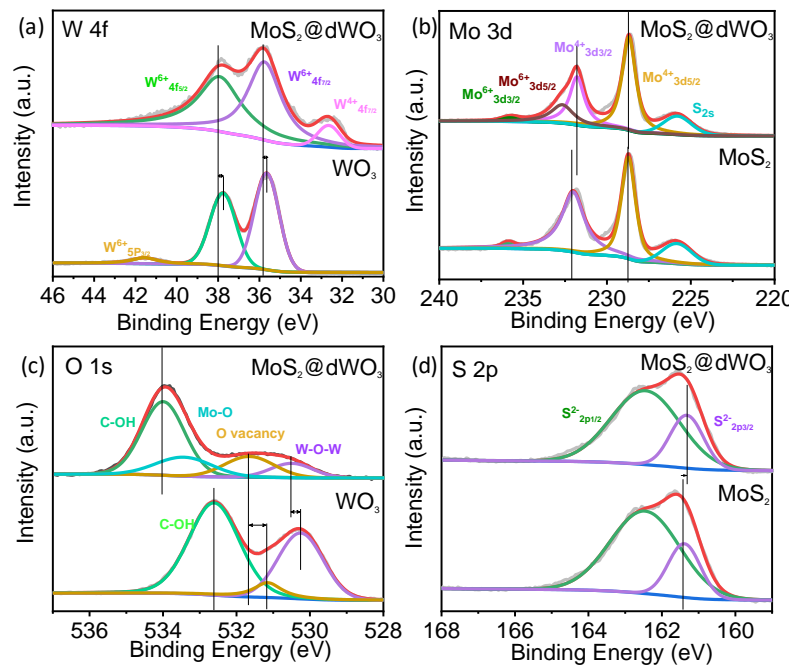


**Figure 2.** X-ray photoelectron spectrum of MoS<sub>2</sub>@dWO<sub>3</sub> heterostructures nanosheets. XPS spectrum of (a) W 4f, (b) Mo 3d, (c) O 1s and (d) S 2p from MoS<sub>2</sub>, WO<sub>3</sub> and MoS<sub>2</sub>@dWO<sub>3</sub>.

In the environment of strong acidity and high current density, the long-term stability and durability of heterostructure catalyst are very important for the practical application of electrochemical hydrogen production. Therefore, the chronoamperometry is used to further perform the process at a constant potential of  $-0.21$  V versus RHE. As shown in Figure 3c, we can observe that the hetero-catalyst runs continuously and stably for 80,000 s at a current density of  $\sim 20$  mA cm<sup>-2</sup> which implying its good durability of heterojunction under HER working condition. Meanwhile, a long-term cycling test of MoS<sub>2</sub>@dWO<sub>3</sub> heterostructure catalyst was also carried out, as shown in Figure 3d. After 5000 cycles at a scan rate of 100 mV s<sup>-1</sup> between  $-0.45$  and  $0.3$  V vs. RHE, the polarization curve before and after the cycle remain similar, and a negligible activity increase is observed, which means that superior stability of prepared heterostructure. Compared to the latest reported MoS<sub>2</sub> based and other nonprecious metal based HER electrocatalysts, ours heterostructure catalyst demonstrate comparable or even more efficient performance, which is more significant for practical application for electrodes in harsh working conditions (Table 1).

As control samples, the pure WO<sub>3</sub> nanosheets were measured and exhibited poor HER activity. The pure MoS<sub>2</sub> nanosheets prepared without WO<sub>3</sub> templates showed a poor long-term stability and durability, in Figure 3e. These experimental results shown that the formation of heterostructure nanosheets is crucial for the enhanced HER performance. Intuitively, by comparing the TEM image of MoS<sub>2</sub> prepared without WO<sub>3</sub>, the effect of WO<sub>3</sub> on the catalyst preparation is expected to be significant for the confined growth of MoS<sub>2</sub> nanosheets. Indeed, the theoretical simulations indicate that the catalytic activity of the edge sites of layered MoS<sub>2</sub> could be effectively impacted by underlying substrates [49]. These results demonstrated that this in situ wet etching strategy is a unique method for constructing heterostructures, which can improve electronic modulation and increase the active edge sites by oxygen incorporation, leading to an enhanced HER performance of MoS<sub>2</sub>-based catalysts.

The excellent electrocatalytic activity and electrical conductivity of heterostructure catalysts was further examined by electrochemical impedance spectroscopy (EIS). As shown as in Figure 3f, the charge transfer resistance ( $R_{ct}$ ) of  $\text{MoS}_2@\text{dWO}_3$  nanosheets is significantly lower than original  $\text{MoS}_2$  and  $\text{WO}_3$  in the EIS, which means that the heterogeneous interface makes the barrier minimize of the charge transfer barrier and improves the electronic conductivity as well. At the same time, it also shown that  $\text{WO}_3$  is an excellent matrix material, which can promote the transmission of protons at the interface [50].

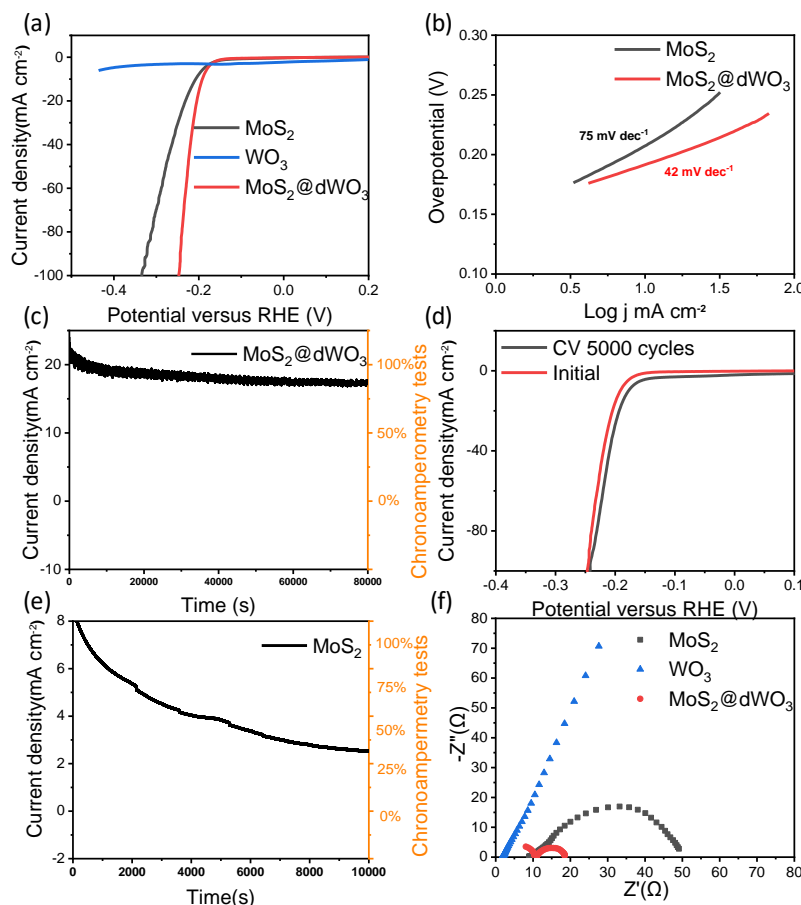


**Figure 3.** Electrocatalytic hydrogen evolution reaction performance. (a) Polarization curves of  $\text{MoS}_2$ ,  $\text{WO}_3$  and  $\text{MoS}_2@\text{dWO}_3$  (b) corresponding Tafel plots of  $\text{MoS}_2$  and  $\text{MoS}_2@\text{dWO}_3$ ; (c) degree of decline of  $\text{MoS}_2@\text{dWO}_3$  through the 80,000 s continuous operation (d) polarization curves of  $\text{MoS}_2@\text{dWO}_3$  initially and after 5000 cyclic voltammetry (CV) sweeps; (e) degree of decline of  $\text{MoS}_2$  through the 10,000 s continuous operation; (f) electrochemical impedance spectroscopy of  $\text{MoS}_2$ ,  $\text{WO}_3$  and  $\text{MoS}_2@\text{dWO}_3$ .

In order to further evaluate the effective electrochemical active surface area (ECSA) of  $\text{MoS}_2$ ,  $\text{WO}_3$  and  $\text{MoS}_2@\text{dWO}_3$ , the electrochemical double-layer capacity ( $C_{dl}$ ) was further examined as shown in Figure 4. The double layer capacitance ( $C_{dl}$ ) of  $\text{MoS}_2@\text{dWO}_3$  is  $83 \text{ mF cm}^{-2}$ , which is higher than that of pristine  $\text{WO}_3$  ( $8 \text{ mF cm}^{-2}$ ) and pure  $\text{MoS}_2$  ( $30 \text{ mF cm}^{-2}$ ). The plots in Figure 4d show that the  $\text{MoS}_2@\text{dWO}_3$  have a large active surface area, which can be attributed to the heterostructure with rich active edge sites. Our experiment measurement indicates a strong dependence in the catalytic activity of the  $\text{MoS}_2$  film on the  $\text{WO}_3$  substrate.

**Table 1.** Comparison of hydrogen evolution reaction (HER) catalytic performance of the different electrocatalysts.

Catalyst	Synthetic Method	$\eta$ (mV) ( $j = 10 \text{ mA cm}^{-2}$ )	Tafel Slope (mV dec $^{-1}$ )	Ref.
Co-MoS <sub>2</sub>	Hydrothermal process	56	32	[35]
MoS <sub>2</sub> /N-RGO-180	Hydrothermal process	56	41	[32]
Cu <sub>7</sub> S <sub>4</sub> @MoS <sub>2</sub>	Hot injection synthesis	133	48	[17]
WS <sub>2</sub> /rGO	Hydrothermal	265	58	[9]
O-MoS <sub>2</sub>	Hydrothermal	300	55	[36]
MoS <sub>2</sub> /rGO	Hydrothermal	150	43.5	[15]
MoS <sub>2</sub> /CoSe <sub>2</sub>	Hydrothermal	75	36	[46]
MoS <sub>2</sub> /CFP	Chemical vapor deposition	168	44	[47]
N,F-MoS <sub>2</sub>	Hydrothermal	210	57	[48]
MoS <sub>2</sub> @dWO <sub>3</sub>	In situ wet etching	191	42	This work

The high HER activity and good stability of the optimized catalyst constructed with heterostructure and designed electronic modulations can be mainly attributed to the following aspects: (i) the heterostructure increases the number of active edges as active sites for hydrogen evolution catalysis; (ii) the WO<sub>3</sub> nanoframes with rich oxygen vacancies serve as an anisotropic substrate to promote electron transport; (iii) the oxygen incorporation in MoS<sub>2</sub> can enhance the overall intrinsic conductivity and help improve electron structure; (iv) the synergistic effect between MoS<sub>2</sub> and WO<sub>3</sub> is beneficial to simultaneously improve the catalytic activity and stability of the material. All in all, in order to achieve high-efficiency electrocatalytic hydrogen evolution, the integrated MoS<sub>2</sub>@dWO<sub>3</sub> heterostructure catalyst were successfully prepared by constructing heterostructural and electronic modulations, paving a new way for improving the activity of various multielement electrocatalysts.

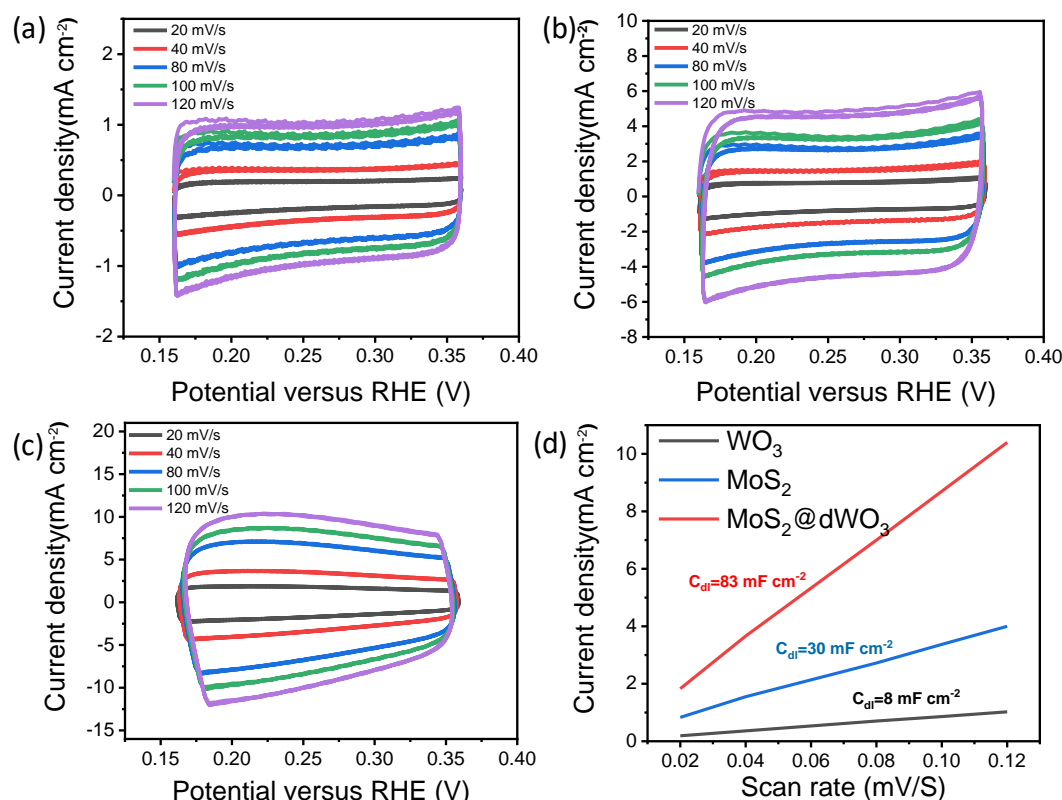


**Figure 4.** Effective electrochemical active surface area tests (ECSA) of (a) WO<sub>3</sub>, (b) MoS<sub>2</sub> and (c) MoS<sub>2</sub>@dWO<sub>3</sub>; (d) electrochemical double-layer capacity ( $C_{dl}$ ) of MoS<sub>2</sub>, WO<sub>3</sub> and MoS<sub>2</sub>@dWO<sub>3</sub>.

### 3. Materials and Methods

#### 3.1. Chemicals and Reagents

Nafion (5% Alfa Aesar, Haverhill, MA, USA),  $(\text{NH}_4)_2\text{MoS}_4$  (99.95%; Alfa Aesar, Haverhill, MA, USA),  $\text{Na}_2\text{WO}_4 \cdot 2\text{H}_2\text{O}$  (99.5%; Alfa Aesar, Haverhill, MA, USA) were obtained from Alfa Aesar (Alfa Aesar, Haverhill, MA, USA). Ethanol, methanol, isopropanol, dimethylformamide, citric acid, hydrochloric, glucose,  $\text{H}_2\text{SO}_4$  (98%) were purchased from Beijing Chemical Regent Company (Beijing Chemical Regent Co., Ltd.; Beijing, China).

#### 3.2. Synthesis of $\text{WO}_3$ Nanosheets

We synthesized  $\text{WO}_3$  nanosheets through a facile hydrothermal method. First, 0.5 mmol of  $\text{Na}_2\text{WO}_4 \cdot 2\text{H}_2\text{O}$  were added to 20 mL of deionized water to form a clear solution, and then 0.75-mmol citric acid and 5-mmol glucose was slowly injected into it. After ultrasonic stirring for 20 min, we slowly dropped 10 mL of HCl (3 M) into the above mixed solution. After magnetic stirring for 60 min, the mixed solution was transferred into a 50-mL Teflon autoclave and heated at 120 °C for 6 h. The precipitates were centrifuged and washed with ethanol and water several times and then dried in vacuum at 60 °C for 4 h.

#### 3.3. Synthesis of $\text{MoS}_2@d\text{WO}_3$ Heterostructure Nanosheets

First, we weighed 5 mg of the  $\text{WO}_3$  nanosheets prepared above and added it into 25 mL DMF under ultrasonication for 10 min at room temperature. Then, under ultrasonic stirring, the solution was added into 5 mL of DMF containing 1 mg of  $(\text{NH}_4)_2\text{MoS}_4$  for 20 min. The mixed solution was then transferred into a 30-mL Teflon autoclave and heated at 180 °C for 10 h. The precipitates were centrifuged and washed with ethanol and water 5 times and then dried in vacuum at 60 °C for 4 h.

#### 3.4. Characterizations

We observed the size and morphology of these prepared nanocomposites through a JEM-1200EX (JEOL; Tokyo, Japan) transmission electron microscope (TEM) operating at 100 kV and JEM-2100 F (JEOL; Tokyo, Japan) transmission electron microscope operating at 200 kV. At the same time, a Bruker AXS D8 Advance X-ray diffractometer (Bruker Daltonics Inc., Karlsruhe, Germany) was used to test the X-ray diffraction (XRD) patterns of these obtained samples with Cu K $\alpha$  radiation ( $\lambda = 1.5418 \text{ \AA}$ ). The operation current and voltage were 40 mA and 40 kV ( $2\theta$  ranging from 5° to 80°), respectively. Finally, in order to explore the combined state of the surface, we used the X-ray photoelectron spectrum (XPS) to measure it on AXIS ULTRA DLD (AXIS; Manchester, UK). We compared the standard binding-energy table and the XPS total spectrum to determine the energy axis of each element. All electrochemical measurements in this article were performed on an electrochemical workstation (CHI 660E, CH Instrument, Inc., Shanghai, China).

#### 3.5. Fabrication of Electrodes

First, we weighed 1.0 mg of carbon black (XC-72) and 2.2 g of  $\text{MoS}_2@d\text{WO}_3$  hybrid nanocrystals, added into 3.0 mL ethanol and then sonicated the mixture for 60-min before transferring the catalyst to the surface of the carbon black. Finally, we took 1 mL of the mixed solution, added isopropanol (750  $\mu\text{L}$ ), ethanol (250  $\mu\text{L}$ ) and nafion (5%, 20  $\mu\text{L}$ ) to form a homogeneous catalyst ink.

Then, we weighed 1.0 mg of carbon black (XC-72) and 2.2 g of  $\text{MoS}_2$  hybrid nanocrystals. To this was added into 3.0 mL ethanol. Then, we sonicated the mixture for 60 min. Finally, we took 1 mL of the mixed solution, added isopropanol (750  $\mu\text{L}$ ), ethanol (250  $\mu\text{L}$ ) and nafion (5%, 20  $\mu\text{L}$ ) to form a homogeneous catalyst ink. The ink of pure  $\text{MoS}_2$  and  $\text{WO}_3$  nanocatalyst was prepared the same way.

Finally, the nanocatalyst ink ( $8.7 \mu\text{L}$ ) was dropped onto the glass carbon (GC) electrode (3-mm in diameter) and then dried for 2 h before electrocatalytic tests, yielding a catalyst loading of  $0.28 \text{ mg cm}^{-2}$  approximately.

### 3.6. Catalytic Measurements

All electrochemical measurements in this article were performed on the electrochemical station (CHI 660E, CH Instrument, Inc., Shanghai, China). The nanocatalyst inks were dropped onto a glassy carbon electrode (GCE) as the working electrode. At the same time, a carbon rod was used as the counter electrode, and a saturated calomel electrode (SCE) was used as reference electrode, respectively. The electrolyte solution was a 0.5-M  $\text{H}_2\text{SO}_4$  solution;  $\text{N}_2$  was passed through for 30 min before the test. The HER performance was tested by linear-sweep voltammetry with sweeping the potential from 0.20 to  $-0.60 \text{ V}$  vs. RHE at a scan rate of  $2 \text{ mV s}^{-1}$ . The cyclic voltammetry was tested under the potential of 0.20 and  $-0.20 \text{ V}$  vs. RHE at the scan rate of  $5 \text{ mV s}^{-1}$ . Electrochemical impedance spectroscopy measurement was carried out from 10,000 Hz to 0.01 Hz. The electrochemical stability was tested by chronoamperometry ( $j-t$ ) at a constant potential of  $-0.21 \text{ V}$  vs. RHE. To estimate the electrochemical active surface area of the sample, cyclic voltammetry was tested under the potential window of 0.16 and  $0.36 \text{ V}$  with various scan rate of 20, 40, 60, 80, 100, 120  $\text{mV s}^{-1}$ .

The saturated calomel electrode (SCE) was used as the reference electrode in the all electrocatalytic measurements. It be calibrated in regard to reversible hydrogen electrode in the 0.5-M  $\text{H}_2\text{SO}_4$  at  $\text{H}_2$ -saturated environment. The Pt wires were used as the working electrode and counter electrode. The cyclic voltammetry (CV) was test at a scan rate of  $1.0 \text{ mV/s}$ , and the average value of potential at which the current crossed zero was the thermodynamic potential for the hydrogen electrode reaction. The CV curve is shown in Figure S3. Therefore, in this work,  $E(\text{RHE}) = E(\text{SCE}) + 0.242 \text{ V}$ .

## 4. Conclusions

In conclusion, we successfully synthesized the  $\text{MoS}_2@\text{dWO}_3$  heterostructure catalyst with enlarged  $\text{MoS}_2$  interlayer spacing and defective  $\text{WO}_3$  substrate using in situ etching method. Importantly, the in situ etching process achieved oxygen-incorporated  $\text{MoS}_2$  via construct hetero-interface at the surface of  $\text{WO}_3$  nanoframes. The  $\text{MoS}_2@\text{dWO}_3$  heterostructure catalyst with rich edge active sites and high overall conductivity could deliver substantially enhanced HER activity and long-term durability in strong acid environment. The resulting nanocomposite exhibits highly activity with a low overpotential of  $191 \text{ mV}$  at  $10 \text{ mA cm}^{-2}$ , with a Tafel slope of  $42 \text{ mV dec}^{-1}$  and long-term stability toward hydrogen evolution reaction. The results indicate that the  $\text{MoS}_2@\text{dWO}_3$  heterostructure catalyst has large potential in water-splitting devices, and our study highlights a promising approach to design and synthesis of other nanostructure catalyst in miscellaneous promising applications.

**Supplementary Materials:** The following are available online at <http://www.mdpi.com/2073-4344/10/9/977/s1>, Figure S1: (a) TEM image and (b) XRD patterns of the pure  $\text{WO}_3$ . Figure S2: TEM image of the pure  $\text{MoS}_2$ . Figure S3: the cyclic voltammetry of RHE calibration.

**Author Contributions:** X.L. performed data analysis and wrote the study. C.W. contributed to the study design and scientific discussion of the results. All authors have read and agreed to the published version of the manuscript.

**Funding:** We acknowledge the financial supports from the Youth Innovation Promotion Association CAS (2020180), CAS STS project (KFJ-STS-ZDTP-068), Shanxi Major Project (20181102026) and the Innovation Fund of Institute of Coal Chemistry (SCJJ-2020-12).

**Acknowledgments:** This work was supported by Junzhong Wang and Leyu Wang.

**Conflicts of Interest:** The authors declare no conflict of interest.

## References

1. Voiry, D.; Yang, J.; Chhowalla, M. Recent strategies for improving the catalytic activity of 2D TMD nanosheets toward the hydrogen evolution reaction. *Adv. Mater.* **2016**, *28*, 6197–6206. [CrossRef]

2. Jin, H.; Guo, C.; Liu, X.; Liu, J.; Vasileff, A.; Jiao, Y.; Zheng, Y.; Qiao, S.-Z. Emerging two-dimensional nanomaterials for electrocatalysis. *Chem. Rev.* **2018**, *118*, 6337–6408. [[CrossRef](#)] [[PubMed](#)]
3. Tan, C.; Zhang, H. Two-dimensional transition metal dichalcogenide nanosheet-based composites. *Chem. Soc. Rev.* **2015**, *44*, 2713–2731. [[CrossRef](#)]
4. Zheng, Y.; Jiao, Y.; Li, L.H.; Xing, T.; Chen, Y.; Jaroniec, M.; Qiao, S.Z. Toward design of synergistically active carbon-based catalysts for electrocatalytic hydrogen evolution. *ACS Nano* **2014**, *8*, 5290–5296. [[CrossRef](#)] [[PubMed](#)]
5. Fu, Q.; Han, J.; Wang, X.; Xu, P.; Yao, T.; Zhong, J.; Zhong, W.; Liu, S.; Gao, T.; Zhang, Z.; et al. 2D transition metal dichalcogenides: Design, modulation, and challenges in electrocatalysis. *Adv. Mater.* **2020**. [[CrossRef](#)] [[PubMed](#)]
6. Lu, Q.; Yu, Y.; Ma, Q.; Chen, B.; Zhang, H. 2D transition-metal-dichalcogenide-nanosheet-based composites for photocatalytic and electrocatalytic hydrogen evolution reactions. *Adv. Mater.* **2016**, *28*, 1917–1933. [[CrossRef](#)]
7. Liu, C.; Wang, L.; Tang, Y.; Luo, S.; Liu, Y.; Zhang, S.; Zeng, Y.; Xu, Y. Vertical single or few-layer MoS<sub>2</sub> nanosheets rooting into TiO<sub>2</sub> nanofibers for highly efficient photocatalytic hydrogen evolution. *Appl. Catal. B-Environ.* **2015**, *164*, 1–9. [[CrossRef](#)]
8. Guo, J.; Huo, F.; Cheng, Y.; Xiang, Z. PAF-1 as oxygen tank to in -situ synthesize edge -exposed O-MoS<sub>2</sub> for highly efficient hydrogen evolution. *Catal. Today* **2020**, *347*, 56–62. [[CrossRef](#)]
9. Yang, L.; Zhu, X.; Xiong, S.; Wu, X.; Shan, Y.; Chu, P.K. Synergistic WO<sub>3</sub>·2H<sub>2</sub>O nanoplates/WS<sub>2</sub> hybrid catalysts for high-efficiency hydrogen evolution. *ACS Appl. Mater. Interfaces* **2016**, *8*, 13966–13972. [[CrossRef](#)]
10. Zhang, N.; Li, X.; Liu, Y.; Long, R.; Li, M.; Chen, S.; Qi, Z.; Wang, C.; Song, L.; Jiang, J.; et al. Defective tungsten oxide hydrate nanosheets for boosting aerobic coupling of amines: Synergistic catalysis by oxygen vacancies and bronsted acid sites. *Small* **2017**, *13*, 1701354. [[CrossRef](#)]
11. Jain, A.; Sadan, M.B.; Ramasubramaniam, A. Promoting active sites for hydrogen evolution in MoSe<sub>2</sub> via transition-metal dopin. *J. Phys. Chem. C* **2020**, *124*, 12324–12336. [[CrossRef](#)]
12. Luo, J.; Xu, P.; Zhang, D.; Wei, L.; Zhou, D.; Xu, W.; Li, J.; Yuan, D. Synthesis of 3D-MoO<sub>2</sub> microsphere supported MoSe<sub>2</sub> as an efficient electrocatalyst for hydrogen evolution reaction. *Nanotechnology* **2017**, *28*, 12. [[CrossRef](#)] [[PubMed](#)]
13. Chen, B.; Liu, E.; He, F.; Shi, C.; He, C.; Li, J.; Zhao, N. 2D sandwich-like carbon-coated ultrathin TiO<sub>2</sub>@defect-rich MoS<sub>2</sub> hybrid nanosheets: Synergistic-effect-promoted electrochemical performance for lithium ion batteries. *Nano Energy* **2016**, *26*, 541–549. [[CrossRef](#)]
14. Fu, W.; He, H.; Zhang, Z.; Wu, C.; Wang, X.; Wang, H.; Zeng, Q.; Sun, L.; Wang, X.; Zhou, J.; et al. Strong interfacial coupling of MoS<sub>2</sub>/g-C<sub>3</sub>N<sub>4</sub> van de Waals solids for highly active water reduction. *Nano Energy* **2016**, *27*, 44–50. [[CrossRef](#)]
15. Sun, Y.; Alimohammadi, F.; Zhang, D.; Guo, G. Enabling colloidal synthesis of edge-oriented MoS<sub>2</sub> with expanded interlayer spacing for enhanced HER catalysis. *Nano Lett.* **2017**, *17*, 1963–1969. [[CrossRef](#)]
16. Ye, W.; Ren, C.; Liu, D.; Wang, C.; Zhang, N.; Yan, W.; Song, L.; Xiong, Y. Maneuvering charge polarization and transport in 2H-MoS<sub>2</sub> for enhanced electrocatalytic hydrogen evolution reaction. *Nano Res.* **2016**, *9*, 2662–2671. [[CrossRef](#)]
17. Xu, J.; Cui, J.; Guo, C.; Zhao, Z.; Jiang, R.; Xu, S.; Zhuang, Z.; Huang, Y.; Wang, L.; Li, Y. Ultrasmall Cu<sub>7</sub>S<sub>4</sub> @MoS<sub>2</sub> hetero-nanoframes with abundant active edge sites for ultrahigh-performance hydrogen evolution. *Angew. Chem. Int. Ed. Engl.* **2016**, *55*, 6502–6505. [[CrossRef](#)]
18. Jiang, R.; He, C.; Guo, C.; Chen, W.; Luo, J.; Chen, Y.; Wang, L. Edge-contact geometry and anion-deficit construction for activating ultrathin MoS<sub>2</sub> on W<sub>17</sub>O<sub>47</sub> in the hydrogen evolution reaction. *Inorg. Chem.* **2019**, *58*, 11241–11247. [[CrossRef](#)]
19. Singh, A.K.; Kumar, P.; Late, D.J.; Kumar, A.; Patel, S.; Singh, J. 2D layered transition metal dichalcogenides (MoS<sub>2</sub>): Synthesis, applications and theoretical aspects. *Appl. Mater. Today* **2018**, *13*, 242–270. [[CrossRef](#)]
20. Liu, B.; Wang, S.; Mo, Q.; Peng, L.; Cao, S.; Wang, J.; Wu, C.; Li, C.; Guo, J.; Liu, B.; et al. Epitaxial MoS<sub>2</sub> nanosheets on nitrogen doped graphite foam as a 3D electrode for highly efficient electrochemical hydrogen evolution. *Electrochim. Acta* **2018**, *292*, 407–418. [[CrossRef](#)]
21. Ai, K.; Ruan, C.; Shen, M.; Lu, L. MoS<sub>2</sub> nanosheets with widened interlayer spacing for high-efficiency removal of mercury in aquatic systems. *Adv. Funct. Mater.* **2016**, *26*, 5542–5549. [[CrossRef](#)]

22. Tan, C.; Cao, X.; Wu, X.-J.; He, Q.; Yang, J.; Zhang, X.; Chen, J.; Zhao, W.; Han, S.; Nam, G.-H.; et al. Recent advances in ultrathin two-dimensional nanomaterials. *Chem. Rev.* **2017**, *117*, 6225–6331. [CrossRef] [PubMed]
23. Wang, J.; Wang, W.; Wang, Z.; Chen, J.G.; Liu, C.-j. Porous  $\text{MS}_2/\text{MO}_2$  ( $\text{M} = \text{W}, \text{Mo}$ ) nanorods as efficient hydrogen evolution reaction catalysts. *Acs. Catal.* **2016**, *6*, 6585–6590. [CrossRef]
24. Geng, S.; Yang, W.; Yu, Y.S. Building  $\text{MoS}_2/\text{S}$ -doped g-C<sub>3</sub>N<sub>4</sub> layered heterojunction electrocatalysts for efficient hydrogen evolution reaction. *J. Catal.* **2019**, *375*, 441–447. [CrossRef]
25. Sivasankaran, R.P.; Rockstroh, N.; Kreyenschulte, C.R.; Bartling, S.; Lund, H.; Acharjya, A.; Junge, H.; Thomas, A.; Brueckner, A. Influence of  $\text{MoS}_2$  on activity and stability of carbon nitride in photocatalytic hydrogen production. *Catalysts* **2019**, *9*, 695. [CrossRef]
26. Kusmierenk, E. Evaluating the effect of  $\text{WO}_3$  on electrochemical and corrosion properties of  $\text{TiO}_2\text{-RuO}_2$ -coated titanium anodes with low content of  $\text{RuO}_2$ . *Electrocatalysis* **2020**, *11*, 555–566. [CrossRef]
27. Lu, H.; Chen, X.; Dai, W.; Zhang, K.; Liu, C.; Dong, H. Prickly pear-like three-dimensional porous  $\text{MoS}_2$ : Synthesis, characterization and advanced hydrogen evolution reaction. *Catalysts* **2018**, *8*, 580. [CrossRef]
28. Yang, S.-Z.; Gong, Y.; Manchanda, P.; Zhang, Y.-Y.; Ye, G.; Chen, S.; Song, L.; Pantelides, S.T.; Ajayan, P.M.; Chisholm, M.F.; et al. Rhodium-doped and stabilized  $\text{MoS}_2$  atomic layers with basal-plane catalytic activity. *Adv. Mater.* **2018**, *30*, 1803477. [CrossRef] [PubMed]
29. Guo, M.; Xing, Z.; Zhao, T.; Qiu, Y.; Tao, B.; Li, Z.; Zhou, W. Hollow flower-like polyhedral alpha- $\text{Fe}_2\text{O}_3$ /defective  $\text{MoS}_2/\text{Ag}$  Z-scheme heterojunctions with enhanced photocatalytic-Fenton performance via surface plasmon resonance and photothermal effects. *Appl. Catal. B-Environ.* **2020**, *272*, 118978. [CrossRef]
30. Zhou, Q.; Feng, J.; Peng, X.; Zhong, L.; Sun, R. Porous carbon coupled with an interlaced MoP- $\text{MoS}_2$  heterojunction hybrid for efficient hydrogen evolution reaction. *J. Energy Chem.* **2020**, *45*, 45–51. [CrossRef]
31. Chen, R.; Song, Y.; Wang, Z.; Gao, Y.; Sheng, Y.; Shu, Z.; Zhang, J.; Li, X.a. Porous nickel disulfide/reduced graphene oxide nanohybrids with improved electrocatalytic performance for hydrogen evolution. *Catal. Commun.* **2016**, *85*, 26–29. [CrossRef]
32. Tang, Y.-J.; Wang, Y.; Wang, X.-L.; Li, S.-L.; Huang, W.; Dong, L.-Z.; Liu, C.-H.; Li, Y.-F.; Lan, Y.-Q. Molybdenum disulfide/nitrogen-doped reduced graphene oxide nanocomposite with enlarged interlayer spacing for electrocatalytic hydrogen evolution. *Adv. Energy Mater.* **2016**, *6*, 1600116. [CrossRef]
33. Wang, H.; Ouyang, L.; Zou, G.; Sun, C.; Hu, J.; Xiao, X.; Gao, L. Optimizing  $\text{MoS}_2$  edges by alloying isovalent W for robust hydrogen evolution activity. *Acs. Catal.* **2018**, *8*, 9529–9536. [CrossRef]
34. Zhang, X.; Lai, Z.; Tan, C.; Zhang, H. Solution-processed two-dimensional  $\text{MoS}_2$  nanosheets: Preparation, hybridization, and applications. *Angew. Chem. Int. Ed.* **2016**, *55*, 8816–8838. [CrossRef] [PubMed]
35. Liu, P.; Zhu, J.; Xi, P.; Tao, K.; Gao, D. P dopants triggered new basal plane active sites and enlarged interlayer spacing in  $\text{MoS}_2$  nanosheets toward electrocatalytic hydrogen evolution. *ACS Energy Lett.* **2017**, *2*, 745–752. [CrossRef]
36. Xie, J.; Zhang, J.; Li, S.; Grote, F.; Zhang, X.; Zhang, H.; Wang, R.; Lei, Y.; Pan, B.; Xie, Y. Controllable disorder engineering in oxygen-incorporated  $\text{MoS}_2$  ultrathin nanosheets for efficient hydrogen evolution. *J. Am. Chem. Soc.* **2013**, *135*, 17881–17888. [CrossRef]
37. Yang, L.; Liu, P.; Li, J.; Xiang, B. Two-dimensional material molybdenum misulfides as electrocatalysts for hydrogen evolution. *Catalysts* **2017**, *7*, 285. [CrossRef]
38. Latorre-Sánchez, M.; Esteve-Adell, I.; Primo, A.; García, H. Innovative preparation of  $\text{MoS}_2$ -graphene heterostructures based on alginate containing  $(\text{NH}_4)_2\text{MoS}_4$  and their photocatalytic activity for  $\text{H}_2$  generation. *Carbon* **2015**, *81*, 587–596. [CrossRef]
39. Joe, J.; Bae, C.; Kim, E.; Ho, T.A.; Yang, H.; Park, J.H.; Shin, H. Mixed-phase (2H and 1T)  $\text{MoS}_2$  catalyst for a highly efficient and stable Si photocathode. *Catalysts* **2018**, *8*, 580. [CrossRef]
40. Gao, Y.; Wang, K.; Song, H.; Wu, H.; Yan, S.; Xu, X.; Shi, Y. Fabrication of C/Co- $\text{FeS}_2/\text{CoS}_2$  with highly efficient hydrogen evolution reaction. *Catalysts* **2019**, *9*, 556. [CrossRef]
41. Hong, S.; Rhee, C.K.; Sohn, Y. Photoelectrochemical hydrogen evolution and  $\text{CO}_2$  reduction over  $\text{MoS}_2/\text{Si}$  and  $\text{MoSe}_2/\text{Si}$  nanostructures by combined photoelectrochemical deposition and rapid-thermal annealing process. *Catalysts* **2019**, *9*, 494. [CrossRef]
42. Zhou, J.; Fang, G.; Pan, A.; Liang, S. Oxygen-incorporated  $\text{MoS}_2$  nanosheets with expanded interlayers for hydrogen evolution reaction and pseudocapacitor applications. *Acs. Appl. Mater. Interfaces* **2016**, *8*, 33681–33689. [CrossRef]

43. Reddy, B.M.; Sreekanth, P.M.; Yamada, Y.; Xu, Q.; Kobayashi, T. Surface characterization of sulfate, molybdate and tungstate promoted  $\text{TiO}_2\text{-ZrO}_2$  solid acid catalysts by XPS and other techniques. *Appl. Catal. A. Gen.* **2002**, *228*, 269–278. [[CrossRef](#)]
44. Jin, Q.; Liu, N.; Dai, C.; Xu, R.; Wu, B.; Yu, G.; Chen, B.; Du, Y. H-2-directing strategy on in situ synthesis of Co-MoS<sub>2</sub> with highly expanded interlayer for elegant HER activity and its mechanism. *Adv. Energy Mater.* **2020**, *10*, 2000291. [[CrossRef](#)]
45. Liu, Y.; Luo, X.; Zhou, C.; Du, S.; Zhen, D.; Chen, B.; Li, J.; Wu, Q.; Iru, Y.; Chen, D. A modulated electronic state strategy designed to integrate active HER and OER components as hybrid heterostructures for efficient overall water splitting. *Appl. Catal. B. Environ.* **2020**, *260*, 118197. [[CrossRef](#)]
46. Gao, M.R.; Liang, J.X.; Zheng, Y.R.; Xu, Y.F.; Jiang, J.; Gao, Q.; Li, J.; Yu, S.H. An efficient molybdenum disulfide/cobalt diselenide hybrid catalyst for electrochemical hydrogen generation. *Nat. Commun.* **2015**, *6*, 5982. [[CrossRef](#)] [[PubMed](#)]
47. Wang, H.; Lu, Z.; Xu, S.; Kong, D.; Cha, J.J.; Zheng, G.; Hsu, P.; Yan, K.; Brandshaw, D.; Prinz, F.B.; et al. Electrochemical tuning of vertically aligned MoS<sub>2</sub> nanofilms and its application in improving hydrogen evolution reaction. *Proc. Natl. Acad. Sci. USA* **2013**, *110*, 19701. [[CrossRef](#)]
48. Wang, Y.; Liu, S.; Hao, X.; Zhou, J.; Song, D.; Wang, D.; Hou, L.; Gao, F. Fluorine- and nitrogen-codoped MoS<sub>2</sub> with a catalytically active basal plane. *Acs. Appl. Mater. Interfaces* **2017**, *9*, 27715–27719. [[CrossRef](#)]
49. Posudievsky, O.Y.; Kozarenko, O.A.; Dyadyun, V.S.; Koshechko, V.G.; Pokhodenko, V.D. Efficient mechanochemical preparation of graphene-like molybdenum disulfide and graphene-based composite electrocatalysts for hydrogen evolution reaction. *Electrocatalysis* **2019**, *10*, 477–488. [[CrossRef](#)]
50. Shibli, S.M.A.; Anupama, V.R.; Arun, P.S.; Jineesh, P.; Suji, L. Synthesis and development of nano WO<sub>3</sub> catalyst incorporated Ni-P coating for electrocatalytic hydrogen evolution reaction. *Int. J. Hydrol. Energy* **2016**, *41*, 10090–10102. [[CrossRef](#)]



© 2020 by the authors. Licensee MDPI, Basel, Switzerland. This article is an open access article distributed under the terms and conditions of the Creative Commons Attribution (CC BY) license (<http://creativecommons.org/licenses/by/4.0/>).